Abdominal Radiology (2019) 44:3336–3349
https://doi.org/10.1007/s00261-019-02122-z

KIDNEYS, URETERS, BLADDER, RETROPERITONEUM

Role of MR texture analysis in histological subtyping and grading of renal cell carcinoma: a preliminary study

Ankur Goyal[1] · Abdul Razik[1] · Devasenathipathy Kandasamy[1] · Amlesh Seth[2] · Prasenjit Das[3] · Balaji Ganeshan[4] · Raju Sharma[1]

Published online: 12 July 2019

Abstract

Purpose The study evaluated the usefulness of magnetic resonance imaging (MRI) texture parameters in differentiating clear cell renal carcinoma (CC-RCC) from non-clear cell carcinoma (NC-RCC) and in the histological grading of CC-RCC.

Materials and methods After institutional ethical approval, this retrospective study analyzed 33 patients with 34 RCC masses (29 CC-RCC and five NC-RCC; 19 low-grade and 10 high-grade CC-RCC), who underwent MRI between January 2011 and December 2012 on a 1.5-T scanner (Avanto, Siemens, Erlangen, Germany). The MRI protocol included T2-weighted imaging (T2WI), diffusion-weighted imaging [DWI; at b 0, 500 and 1000 s/mm^2 with apparent diffusion coefficient (ADC) maps] and T1-weighted pre and postcontrast [corticomedullary (CM) and nephrographic (NG) phase] acquisition. MR texture analysis (MRTA) was performed using the TexRAD research software (Feedback Medical Ltd., Cambridge, UK) by a single reader who placed free-hand polygonal region of interest (ROI) on the slice showing the maximum viable tumor. Filtration histogram-based texture analysis was used to generate six first-order statistical parameters [mean intensity, standard deviation (SD), mean of positive pixels (MPP), entropy, skewness and kurtosis] at five spatial scaling factors (SSF) as well as on the unfiltered image. Mann–Whitney test was used to compare the texture parameters of CC-RCC versus NC-RCC, and high-grade versus low-grade CC-RCC. P value < 0.05 was considered significant. A 3-step feature selection was used to obtain the best texture metrics for each MRI sequence and included the receiver-operating characteristic (ROC) curve analysis and Pearson's correlation test.

Results The best performing texture parameters in differentiating CC-RCC from NC-RCC for each sequence included (area under the curve in parentheses): entropy at SSF 4 (0.807) on T2WI, SD at SSF 4 (0.814) on DWI b500, SD at SSF 6 (0.879) on DWI b1000, mean at SSF 0 (0.848) on ADC, skewness at SSF 2 (0.854) on T1WI and skewness at SSF 3 (0.908) on CM phase. In differentiating high from low-grade CC-RCC, the best parameters were: entropy at SSF 6 (0.823) on DWI b1000, mean at SSF 3 (0.889) on CM phase and MPP at SSF 5 (0.870) on NG phase.

Conclusion Several MR texture parameters showed excellent diagnostic performance (AUC > 0.8) in differentiating CC-RCC from NC-RCC, and high-grade from low-grade CC-RCC. MRTA could serve as a useful non-invasive tool for this purpose.

Keywords Renal cell carcinoma · Fuhrman grade · Magnetic resonance imaging · Radiomics · Texture analysis

Introduction

Renal cell carcinoma (RCC) is the 16th most common cancer worldwide, accounting for 2.2% of all newly diagnosed cancers [1]. About 17% of the cases are found to be metastatic at presentation [2]. The most important prognostic factors are the TNM stage and Fuhrman's nuclear grade, the latter consisting of four grades (low grade: 1 and 2; high grade: 3 and 4) based on nuclear morphology and pleomorphism [3]. Higher grades are associated with poor prognosis [4]. Clear cell RCC (CC-RCC) accounts for the majority

✉ Raju Sharma
raju152@yahoo.com

[1] Department of Radiology, All India Institute of Medical Sciences, Ansari Nagar, New Delhi 110029, India

[2] Department of Urology, All India Institute of Medical Sciences, Ansari Nagar, New Delhi, India

[3] Department of Pathology, All India Institute of Medical Sciences, Ansari Nagar, New Delhi, India

[4] Institute of Nuclear Medicine, University College London, London, UK

(75%) of cases, followed by papillary, chromophobe, collecting duct, medullary and unclassified types which are collectively labeled as non-clear cell RCC (NC-RCC) [5]. CC-RCC has higher mortality than NC-RCC. CC-RCC primarily expresses mutations of the Von Hippel-Lindau (VHL) gene or the mammalian target of rapamycin (mTOR) pathway and thus, several targeted-therapy agents (tyrosine kinase inhibitors such as sunitinib and mTOR inhibitors such as everolimus) have been used successfully in the management of these tumors [6]. Hence, RCC subtyping and grading provides significant prognostic information and helps to guide therapy.

Currently, this information is obtained from histopathological evaluation of the resected specimen since most of the suspected RCCs undergo surgery. In case of metastatic disease, biopsy is performed to obtain the same information. Biopsy carries a small risk (3.5%) of hemorrhage and remote risk (1:10,000) of tract seeding [7, 8]. In addition, there has been an increasing interest in exploring the potential of neoadjuvant chemotherapy since it could treat micrometastasis and reduce tumor size, thereby enabling a more conservative surgery [9]. Hence, there is a need for preoperative prediction of tumor subtype and grade using non-invasive tools such as imaging. Diffusion-weighted imaging (DWI) and perfusion MRI were the first modalities to be used for this purpose [10, 11].

Of late, a lot of interest has emerged in radiomics and texture analysis (TA). Radiomics is the science of extraction, analysis and interpretation of quantitative imaging parameters beyond what can be subjectively assessed by the human eye. These findings could reflect microscopic features of tumors and provide information useful in tumor subtyping and grading, genetic mapping and prediction of early treatment response. Texture analysis assesses tumor heterogeneity at the pixel level by evaluating the distribution and spatial relationship of grayscale values [12].

Several studies have used TA to subtype and grade RCC on contrast-enhanced CT images [13–20]. Many authors have also used machine learning algorithms in interpreting and validating the data to generate classifiers which could enhance the findings of individual metrics and save time in the process. In the present study, we explored MR texture analysis (MRTA) as a tool for subtyping and grading RCC. MRI provides multiple paradigms for assessment of the morphology and functional microenvironment of renal tumors. Hence, it is likely that MRTA could provide more robust metrics in comparison to CT. Being a radiation-free modality, MRI is likely to be used more extensively in the future, particularly in children and those on follow-up. Till date, only one study has evaluated MR texture analysis in RCC [21]. Hence, the purpose of this study was to evaluate the role of MRTA in the differentiation of CC-RCC from NC-RCC and high-grade CC-RCC from low-grade CC-RCC.

Methodology

Patient selection

A retrospective review of the MRI records between January 2011 and December 2012 was done to look for adult patients with suspected RCC. These patients were part of an ethically approved study to evaluate renal lesions using CT and MRI and informed consent had been taken from all the patients. This dataset yielded a consecutive sample of 39 patients who underwent MRI and were subsequently proven to have renal cell carcinoma on histopathological evaluation of the biopsy or nephrectomy specimen. Among these, two were excluded since their complete imaging data could not be retrieved from the local picture archiving and communications system (PACS). Four patients were excluded since their tumors were predominantly cystic and had insufficient solid component (< 1 cm^2) where a region of interest (ROI) could be drawn. Finally, a total of 33 patients were included. Among these, one patient had two tumors. Thus, a total of 34 tumors underwent texture analysis.

MRI acquisition parameters

All the MR examinations were performed on a 1.5-T scanner (Avanto, Siemens, Erlangen, Germany) using a 16-channel phased array torso coil. Non-contrast sequences included axial and coronal fat-suppressed T2-weighted turbo spine-echo (T2W TSE) acquired in multiple breath-holds, axial T1-weighted dual gradient-echo in-phase (TE: 4.76 ms) and out-of-phase (TE: 2.34 ms) images acquired in multiple breath-holds, axial and coronal true fast imaging with steady-state precession (TrueFISP) in a single breath-hold and diffusion-weighted images (DWI). For DWI, fat-suppressed echo-planar imaging (EPI) was used to acquire the images in the axial plane using diffusion-sensing gradients in all the three orthogonal planes at b values of 0, 500 and 1000 s/mm^2. Navigator-triggered respiratory gating was used to acquire the images. Following acquisition, a pixel-wise apparent diffusion coefficient (ADC) map was generated by the inbuilt software using b values of 0 and 500 s/mm^2.

All patients with eGFR above 60 mL/min/1.73 m^2 underwent multiphase contrast-enhanced study. Nine patients (10 tumors) did not undergo postcontrast imaging due to deranged renal parameters. For the remaining 24 patients, contrast imaging was performed using fat-suppressed 3D T1-weighted volume interpolated breath-hold examination (VIBE) sequence in the axial plane after injection of gadobenate dimeglumine (Multihance,

Bracco, Milan, Italy), at the rate of 2 mL/s followed by 20 mL saline chase using a dual-head pressure injector. The bolus-tracking method was used to time the multiphase acquisition at 40–50 s [corticomedullary (CM) phase], 80–100 s [nephrographic (NG) phase] and 180 s (delayed phase). Precontrast images were also acquired for the purpose of subtraction and postcontrast coronal acquisition was also done. The imaging protocol is described in Table 1.

Feature extraction: MRTA

Both the non-contrast and postcontrast images were available for TA in 24 patients, whereas in the remaining 9 patients (10 tumors), only the non-contrast images were available. The texture analysis was performed by a single radiologist (A.R., with 5 years of experience in diagnostic imaging) who was blinded to the final histopathologic diagnosis. For the analysis, the axial dataset of the fat-suppressed pre-contrast T1-VIBE, T2W TSE images, DWI images at b500 and 1000 s/mm^2, ADC map as well as the postcontrast (CM and NG phase) T1-VIBE images were used. The image data were uploaded onto the TexRAD software (Feedback Medical Ltd., Cambridge, UK- www.fbkmed.com). The NG phase T1-VIBE images were screened initially to map the distribution of the enhancing, viable tumor component. Subsequently, single representative slice which showed the maximum amount of viable tumor component was chosen and a free-hand polygonal ROI of minimum size 1 cm^2 was drawn within the tumor (Fig. 1a). Care was taken to avoid extending the margins of the ROI into the peripheral 2–3 mm of the tumor to avoid potential errors arising from volume averaging and inclusion of perirenal fat. Predominantly, cystic tumors not having contiguous solid component of at least 1 cm^2 were excluded. ROIs were similarly placed on the other sequences at the same anatomical section using the NG phase image as the reference to avoid mapping the necrotic portions of the tumor. Necrotic areas were avoided in an effort to remove the confounding effect of macroscopic necrosis, so that the texture parameters would truly reflect microscopic heterogeneity. Multiple ROIs or volumetric ROI were not used since they were cumbersome, time-consuming and more prone to compounding of errors resulting from incorrect drawing of the ROI and inclusion of the necrotic component.

MRTA using TexRAD comprises of a filtration-histogram technique, where an initial Laplacian of Gaussian spatial band-pass filter is applied to extract and enhance features of different sizes corresponding to the spatial scaling factors (SSF) applied. The filtration step further reduces the effects of photon noise on texture quantification. Five spatial scale filters (SSF) were used- 2 mm (fine texture), 3, 4 and 5 mm (medium texture) as well as 6 mm (coarse texture) (Fig. 1b–d). In addition, the unfiltered images (SSF: 0 mm) were also analyzed. Subsequently, a pixel intensity distribution histogram was generated and texture feature extraction was performed to derive six quantitative first-order statistical metrics for each SSF: mean intensity (average of the grey-level intensity), standard deviation (SD; dispersion of pixel intensities from the mean), entropy (irregularity or disorder in the distribution of the pixel intensities), mean of positive pixels (MPP), skewness (asymmetry of the histogram) and kurtosis (peakedness of the histogram). Thus, 36 texture variables were obtained for each tumor.

Statistical analysis

Statistical analysis was performed using the IBM SPSS software for Windows, version 24.0 (IBM Corp, Armonk, NY, USA). To compare the differences in texture parameters between CC-RCC and NC-RCC, the non-parametric Mann–Whitney U test was used. To assess any significant association between texture parameters and the different Fuhrman grades (0–4) of CC-RCC, the non-parametric

Table 1 MR-imaging sequences and acquisition parameters

Sequence	TR (ms)	TE (ms)	Slice thickness (mm)	Flip angle (degrees)	No. of averages	FOV (mm)	Matrix
T2W TSE FS axial	2520	100	5	137	1	278×370	288×512
T2W TSE FS coronal	2700	100	5	137	1	410×430	171×256
T1W GRE in-phase	125	4.76	5	70	1	278×370	288×512
T1W GRE out-of-phase	125	2.34	5	70	1	278×370	288×512
True FISP axial	3.4	1.4	5	39	1	263×350	288×512
True FISP coronal	3.4	1.4	5	36	1	380×380	410×512
DWI FS axial (b0, 500, 1000 s/mm^2)	1600	62	7	90	6	249×380	94×192
T1W FS VIBE 3D (axial)	5.1	2.3	3	10	1	253×450	158×512

TR time to repeat, *TE* time to echo, *FOV* field of view, *T2W* T2-weighted, *TSE* turbo spin echo, *FS* Fat-suppressed, *T1W* T1-weighted, *GRE* gradient-recalled echo, *FISP* fast imaging with steady-state precession, *DWI* diffusion-weighted imaging, *VIBE* volume interpolated breath-hold examination

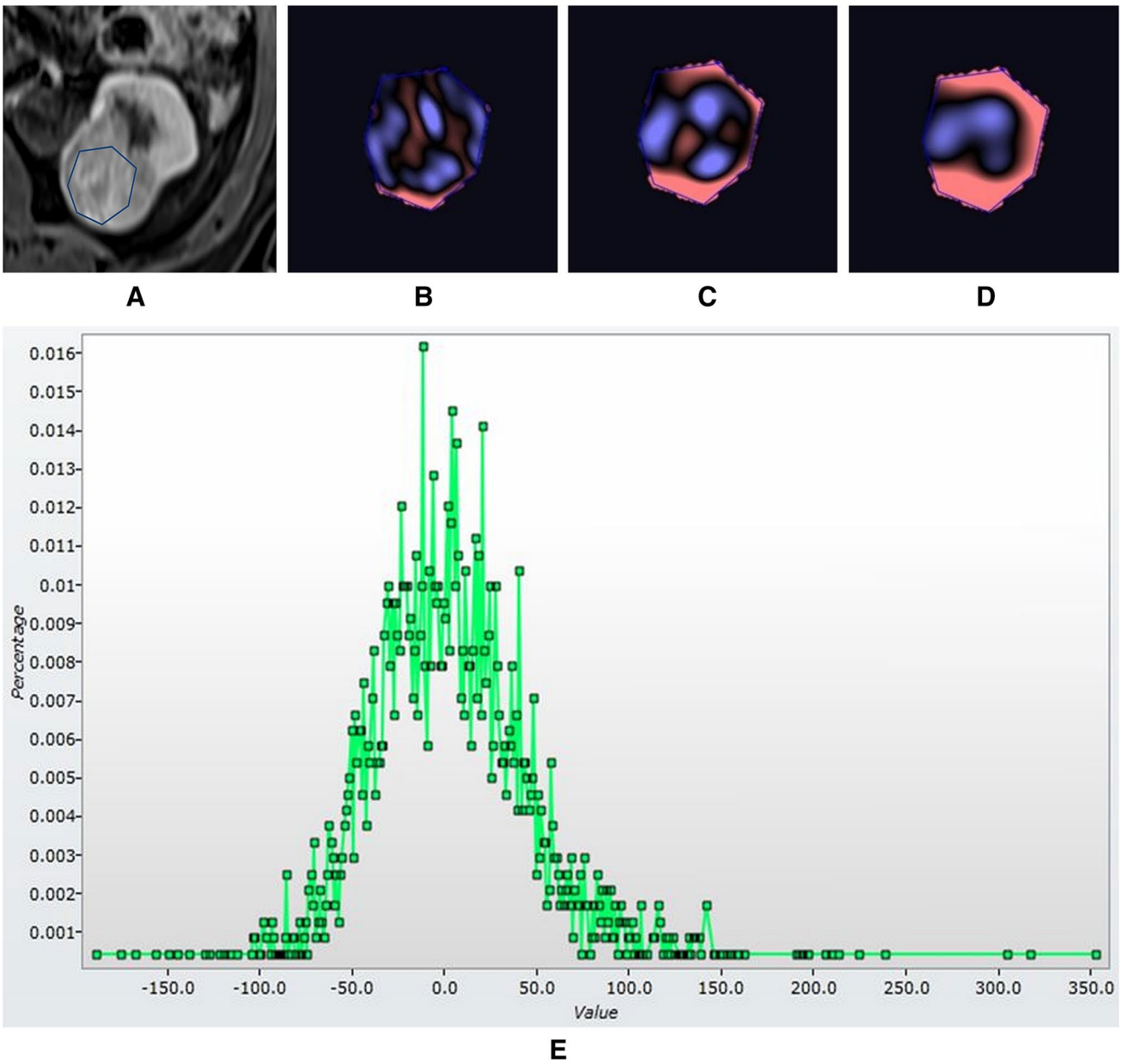

Fig. 1 56-year-old male with low-grade clear cell RCC in the right kidney. **a** Demonstration of ROI placement on the nephrographic (NG) phase MR image. The free-hand polygonal ROI (blue contour) is placed on the slice containing maximum viable component of the tumor, taking care to avoid the peripheral 3 mm and any necrotic component. **b**, **c** and **d** Colour display of the post-filtration texture analysis images at fine (**b**), medium (**c**) and coarse (**d**) spatial scaling factors. **e** A pixel intensity distribution histogram is subsequently generated

Spearman's rank correlation test was performed. A distinction was also sought between the texture parameters of the clinically relevant groupings of tumor grade i.e. high (grades 3 and 4) versus low (grades 1 and 2) grade, using the Mann–Whitney U test. P value < 0.05 was considered significant.

Since the volume of data was large, data reduction was essential to deduce meaningful conclusions. Feature selection was performed using a predefined, three-step approach so as to obtain the best performing metric (parameter) for each MR sequence after removing irrelevant and redundant metrics (Fig. 2). As the first step in differentiating CC-RCC versus NC-RCC and high-grade from low-grade CC-RCC, all parameters which showed significant P value underwent receiver-operating characteristic (ROC) curve analysis to generate the area under the curve (AUC) and optimal cut-off value. Only the parameters which showed a high class separation capacity i.e. AUC > 0.8, were selected. The second

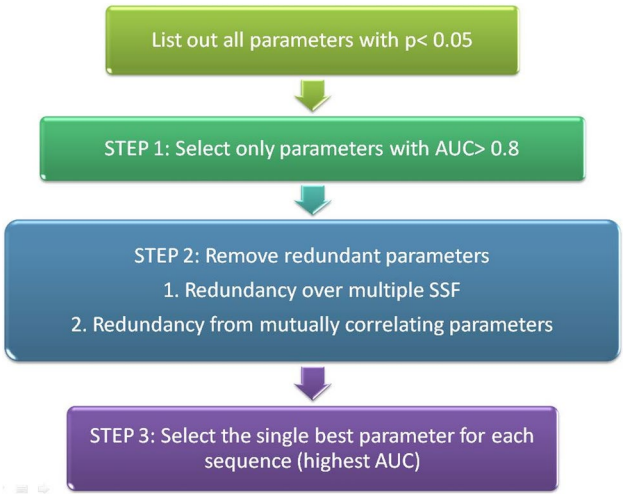

Fig. 2 Flowchart depicting the three-step approach to feature selection

step was targeted at identifying and removing the redundant data. For this, if the same metric showed AUC > 0.8 at multiple SSFs in the same sequence, only the SSF with highest AUC was selected since the texture parameters at different SSF values are known to correlate with each other. If parameters at more than one SSF showed the same AUC, only the one at the higher SSF was retained since higher SSF is known to mitigate photon noise and provide more accurate texture parameters than lower SSF filters. For the remaining parameters in each sequence, Pearson's correlation test was applied to look for mutual correlation. In case a strong mutual correlation ($r > 0.9$) was observed, only the parameter with the highest AUC value was retained. The remaining parameters underwent the third step, where only the parameter with the highest AUC for each sequence was retained as the best performing metric.

Similarly, in differentiating the Fuhrman grades of CC-RCC, all the p values were tabulated and Spearman's correlation coefficient was extracted for the significant *P* values (< 0.05) and only the parameters which showed a correlation coefficient $\rho > 0.8$, were selected for the second step. The second and third steps of feature selection were similar to the previous scenario.

Results

Mean age of the study population (33 patients) was 50.2 years and a male predominance (26 males vs. 7 females) was observed. The study population had a total of 34 RCCs (29 CC-RCCs, four papillary RCCs and one chromophobe RCC). Among CC-RCC, there were 10 high-grade and 19 low-grade tumors. The mean diameter of the tumors was 6.63 ± 3.2 cm and the mean ROI size was 2.6 ± 0.8 cm^2.

Differentiation of CC-RCC from NC-RCC

After Mann–Whitney analysis, the *P* values of all the parameters were tabulated separately for each MR sequence and the metrics with significant *P* value were identified (Table 2). This yielded a total of 25 metrics across all the sequences (three on T2W imaging, five on DWI b500, nine on DWI b1000, five on the ADC maps, one on the unenhanced T1W image, and two on the postcontrast CM phase images). On the NG images, no parameter was observed to be significant in differentiating CC-RCC from NC-RCC.

Subsequently, AUC values of all the parameters which showed a significant p value were tabulated (Table 3). After the first step in feature selection (selecting only those metrics with AUC > 0.8), the number of metrics reduced from 25 to 19. In the second step, for each metric on an MRI sequence, only the SSF with highest AUC was selected thereby reducing the number of metrics to nine (one each on T2W, DWI b500, T1W and CM phase images, two on ADC and three on DWI b1000). After this, for sequences with more than one remaining parameter, the Pearson's correlation test was applied sequence-wise, on which no strong correlation ($r > 0.9$) was observed between the parameters on DWI b1000 images [SD at SSF 6 vs. entropy at SSF 0 ($r = 0.199$), entropy at SSF 0 vs. MPP at SSF 2 ($r = 0.089$) and SD at SSF 6 vs. MPP at SSF 2 ($r = 0.756$)]. On the ADC images, mean and MPP at SSF 0 showed strong correlation ($r = 1.0$), a finding which was expected since ADC maps possess only positive pixels. Hence only mean was retained.

After the third step of data reduction, the following features were selected as the sequence-wise best parameters in distinguishing CC-RCC from NC-RCC: (a) entropy at SSF 4 [AUC: 0.807, 95% confidence interval (CI) 0.664–0.950] on the T2W images (b) SD at SSF 4 (AUC: 0.814, 95% CI 0.577–1.000) on DWI b500 (c) SD at SSF 6 (AUC: 0.879, 95% CI 0.748–1.000) on DWI b1000 (d) mean at SSF 0 (AUC: 0.848, 95% CI 0.609–0.950) on the ADC map (e) skewness at SSF 2 (AUC: 0.854, 95% CI 0.673–1.000) on T1 W images and (f) skewness at SSF 3 (AUC: 0.908, 95% CI 0.782–1.000) on the CM phase images. The optimal cut-off values with their diagnostic performance are shown in Table 3. A box and whisker plot of the single best performing parameter (skewness at SSF3 on the CM phase) is given in Fig. 3.

Correlation of texture parameters with Fuhrman grades of CC-RCC

Forty-six texture parameters showed significant correlation with the Fuhrman grades of RCC. These included four

Table 2 Mann–Whitney U test in the differentiation of CC-RCC from NC-RCC: *P* value of all the evaluated texture parameters, listed MR sequence-wise

SSF	Mean	SD	Entropy	MPP	Skewness	Kurtosis
T2WI						
0	0.888	0.393	0.110	0.888	0.888	0.213
2	0.367	0.448	**0.033**	0.393	0.851	0.777
3	0.603	0.671	**0.029**	0.962	0.420	0.925
4	0.851	0.925	**0.025**	0.741	0.089	0.741
5	0.925	0.925	0.056	0.777	0.232	0.273
6	1.000	0.888	0.089	0.851	0.888	0.135
DWI b 500						
0	0.196	**0.025**	0.273	0.196	0.925	0.539
2	0.925	**0.029**	0.814	0.089	0.420	0.741
3	0.508	**0.044**	0.925	0.135	0.122	0.273
4	0.273	**0.029**	0.962	0.135	0.295	0.110
5	0.122	0.063	1.000	0.149	0.196	**0.038**
6	0.099	0.063	0.962	0.149	0.342	0.080
DWI b 1000						
0	0.213	**0.025**	**0.029**	0.213	0.637	0.110
2	0.637	**0.022**	0.342	**0.033**	0.888	0.477
3	0.342	**0.025**	0.179	**0.038**	0.706	0.342
4	0.448	**0.029**	0.318	0.056	0.671	0.232
5	0.530	**0.010**	0.342	0.071	0.962	0.477
6	0.393	**0.007**	0.273	0.071	0.671	0.814
ADC						
0	**0.012**	0.122	0.295	**0.012**	0.348	0.270
2	0.539	**0.016**	0.342	**0.050**	0.163	0.213
3	1.000	0.163	0.295	0.213	0.149	0.135
4	0.962	0.671	0.393	0.539	0.342	0.080
5	0.706	1.000	0.342	0.508	0.888	0.099
6	0.539	0.777	0.295	0.342	0.925	**0.038**
T1WI						
0	0.126	0.635	0.505	0.126	0.164	0.144
2	0.262	0.262	0.390	0.776	**0.024**	0.547
3	0.144	0.505	0.465	0.924	0.126	0.825
4	0.110	0.547	0.776	0.728	0.505	0.390
5	0.095	0.590	0.635	0.776	0.355	0.505
6	0.110	0.681	0.681	0.547	0.465	1.000
CM phase						
0	0.366	0.505	0.667	0.366	0.667	1.000
2	0.785	0.138	0.162	0.250	0.611	1.000
3	0.505	0.188	0.409	0.188	**0.009**	0.907
4	0.286	0.286	0.667	0.162	**0.009**	0.505
5	0.188	0.324	0.725	0.162	0.097	0.250
6	0.218	0.324	0.725	0.250	0.557	0.785
NG phase						
0	0.183	0.347	0.682	1.000	0.852	0.682
2	0.183	0.794	0.347	1.000	0.388	0.135
3	0.135	0.627	0.347	0.911	0.627	0.347
4	0.157	0.794	0.575	0.737	0.627	0.737
5	0.183	0.431	0.627	0.737	0.682	0.794
6	0.183	0.347	0.682	1.000	0.852	0.682

Parameters showing statistical significance ($P < 0.05$) are highlighted in bold

Table 3 AUC values and diagnostic performance of all the parameters which showed statistical significance ($P < 0.05$) in the differentiation of CC-RCC from NC-RCC, listed MR sequence-wise

Parameter	SSF	AUC	Cut-off	Sensitivity	Specificity	PPV	NPV	Accuracy
T2W								
Entropy	2	0.793	≥5.220	60.7	100	100	31.3	66.7
Entropy	3	0.800	≥5.180	67.9	100	100	35.7	72.7
Entropy	4	**0.807***	≥5.130	71.4	100	100	38.5	75.8
DWI b500								
SD	0	0.814	≤11.260	72.4	100	100	38.5	76.5
SD	2	0.807	≤35.680	82.1	80.0	95.8	44.4	81.8
SD	3	0.793	≤45.190	82.1	80.0	95.8	44.4	81.8
SD	4	**0.814***	≤53.050	85.7	80.0	96.0	50.0	84.8
Kurtosis	5	0.786	≤0.020	71.4	80.0	95.2	33.3	72.7
DWI b1000								
SD	0	0.807	≤7.200	57.1	100	100	29.4	63.6
SD	2	0.821	≤23.700	82.1	80	95.8	44.4	81.8
SD	3	0.821	≤23.120	60.7	100	100	31.3	66.7
SD	4	0.821	≤26.300	67.9	100	100	35.7	72.7
SD	5	0.871	≤28.550	75.0	100	100	41.7	78.8
SD	6	**0.879***	≤26.300	67.9	100	100	35.7	72.7
Entropy	0	**0.800**	≤3.140	53.6	100	100	27.8	60.6
MPP	2	**0.800**	≤20.690	78.6	80.0	95.7	40.0	78.8
MPP	3	0.800	≤18.590	60.7	100	100	31.3	66.7
ADC								
Mean	0	**0.848***	≥1042.41	89.7	80	96.3	57.1	88.2
SD	2	0.724	≥141.980	58.6	80	94.4	25	61.8
MPP	0	**0.848**	≥1042.41	89.7	80	96.3	57.1	88.2
MPP	2	0.779	≥360.850	58.6	100	100	29.4	64.7
Kurtosis	6	0.793	≥−0.420	72.4	100	100	38.5	76.5
T1W								
Skewness	2	**0.854***	≥−0.100	70.8	100	100	36.4	75.0
CM phase								
Skewness	3	**0.908***	≥0.170	78.9	100	100	50	82.6
Skewness	4	0.908	≥0.200	73.7	100	100	44.4	78.3
NG phase								
–	–	–	–	–	–	–	–	–

Parameters remaining after the second step of feature selection are shown in bold. The sequence-wise single best parameters are highlighted with asterisk

parameters on DWI b500 images, six on DWI b1000, nine on ADC map, 13 on the CM phase images and 14 on the NG images (Table 4). However, after the first step of feature selection, none of the metrics showed strong correlation ($\rho > 0.8$).

Differentiation of high-grade from low-grade CC-RCC

On combining the nuclear grades into groups of two (i.e. high and low grades), 49 parameters showed significant difference across all the sequences (Table 5). This included two each on T1W, T2W and DWI b500, 10 on DWI b1000, 11 on the ADC map, 10 on the CM phase images and 12 on the NG phase images.

Next, AUC values of all the significant parameters were tabulated sequence-wise (Table 6). The first step of feature selection reduced the number of metrics from 49 to 16. In the second step, for each metric, only the SSF with the highest AUC was retained, thereby reducing the number of metrics to seven (one on DWI b1000, three each on the CM and NG phase images). However, on the CM phase images, the texture parameter of mean intensity showed the same AUC value at two SSF (0.889 for both SSF 2 and SSF 3). In this case, only the mean at the higher SSF (i.e. SSF 3) was retained. Subsequently, for sequences with more than one remaining parameter, the Pearson's correlation test

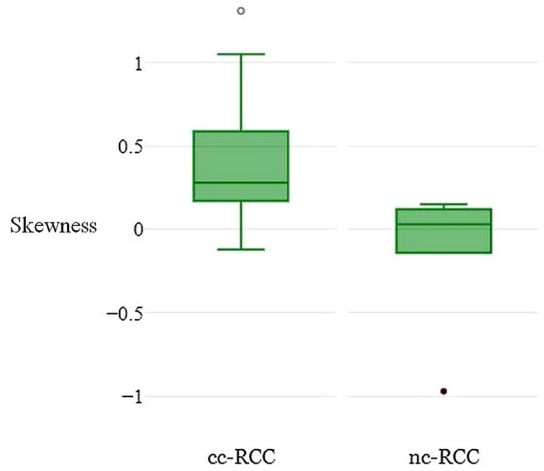

Fig. 3 Box and whisker plot of the best forming parameter in differentiating CC-RCC from NC-RCC (skewness at SSF3 on the corticomedullary phase)

was applied sequence-wise, on which no strong correlation ($r > 0.9$) was observed between mean at SSF 2 versus MPP at SSF 5 ($r = 0.586$) and mean at SSF 3 versus MPP at SSF 5 on the CM phase images ($r = 0.722$); mean at SSF 6 versus SD at SSF 5 ($r = 0.296$), mean at SSF 6 versus MPP at SSF 5 ($r = 0.796$) and SD at SSF 5 versus MPP at SSF 5 ($r = 0.642$) on the NG phase images.

After the third step of data reduction, the following features were selected as the sequence-wise best parameters in distinguishing high-grade from low-grade clear cell RCC: (a) entropy at SSF 6 (AUC: 0.823, 95% CI 0.618–1.000) on DWI b1000 (b) mean at SSF 3 (AUC: 0.889, 95% CI 0.655–1.000) on the CM phase images and (c) MPP at SSF 5 (AUC: 0.870, 95% CI 0.712–1.000) on the NG phase images. The optimal cut-off values with their diagnostic performance are shown in Table 6. A box and whisker plot of the best forming parameter (mean at SSF3 on the CM phase) is given in Fig. 4.

Discussion

Although currently histopathology is the gold standard, for tumor subtype and grade, there is an intensive search for non-invasive imaging biomarkers which can provide prognostic information preoperatively and reduce the need for biopsy. Radiomics has generated significant interest with multiple studies finding a satisfactory diagnostic performance in grading and subtyping RCC on contrast-enhanced CT images using texture analysis [13–20].

In this study, we explored the performance of MRTA in differentiating CC-RCC from NC-RCC and high-grade from low-grade CC-RCC. MRI provides multiple paradigms for assessment of the morphology (T1, T2-weighted and postcontrast images) and functional microenvironment (DWI, perfusion MRI) of tumors. Hence it is likely that MRTA could provide more robust and reliable metrics in comparison to CT texture analysis. Only one published study has previously used MRTA in RCC, where they attempted to differentiate the two subtypes of papillary RCC and observed that addition of TA to qualitative analysis improved the prediction of type 2 tumors [21]. In our study, several texture parameters demonstrated strong diagnostic performance in differentiating CC-RCC from NC-RCC and high-grade from low-grade CC-RCC.

Texture analysis quantifies heterogeneity by assessing the differences in the brightness of the highlighted features from the background signal intensity. Miles et al. has demonstrated how imaging findings are related to texture parameters [22]. SD and entropy, which are measures of dispersion and disorder, respectively, tend to be higher with greater degrees of heterogeneity. On the other hand, kurtosis, which is a measure of the peakedness of the histogram, decreases with greater heterogeneity [17]. Mean and MPP are related to overall brightness, with mean and MPP showing a positive correlation with greater signal intensity and enhancement [17, 23]. An increase in the number of brighter pixels also shifts the tail of the histogram to the right, resulting in positive skewness.

CC-RCC shows greater degree of heterogeneity than NC-RCC on morphologic imaging, attributable to the larger extent of necrosis [17]. Consistent with this logic, T2W images showed higher entropy for CC-RCC in our study, although no such observations were significant on the postcontrast images. CC-RCC also shows higher mean enhancement as compared to papillary RCC which is a hypoenhancing tumor [24]. Consistent with this, CC-RCC showed more positively skewed values than NC-RCC on the postcontrast CM phase images at SSF 3. On DWI, papillary RCC tumors are known to show greater diffusion restriction than CC-RCC [11]. In agreement with this principle, CC-RCC had lower MPP values on DWI b1000 and higher mean values on the ADC map. On DWI, CC-RCC had lower SD and entropy values, suggesting a more homogeneous pattern of diffusion restriction within the pixels.

In the differentiation of tumor grades, high-grade tumors are expected to show greater diffusion restriction and hence, higher mean and MPP with more positive skewness on DWI [25]. However, our study failed to demonstrate any significant difference in this regard, although high-grade tumors showed higher degree of entropy than low-grade tumors on the DWI b1000 images. Due to higher predisposition for necrosis, high-grade tumors show more heterogeneity on morphologic imaging [17]. High-grade tumors showed lower mean and MPP on the CM and NG phase images than low-grade tumors, suggestive of lower net enhancement which could be attributed to greater necrosis at the microscopic

Table 4 Spearman's rank correlation test in the association of MR texture features with the Fuhrman grades of CC-RCC: *P* value of all the evaluated texture parameters, listed MR sequence-wise

SSF	Mean	SD	Entropy	MPP	Skewness	Kurtosis
T2WI						
0	0.258	0.779	0.579	0.258	0.990	0.093
2	0.053	0.365	0.668	0.212	0.585	0.249
3	0.298	0.290	0.648	0.334	0.291	0.787
4	0.804	0.105	0.933	0.334	0.241	0.971
5	0.923	0.104	0.819	0.540	0.653	0.241
6	0.949	0.103	0.910	0.408	0.753	0.175
DWI b 500						
0	**0.021(0.419)**	0.147	0.074	**0.021 (0.419)**	0.354	0.365
2	0.569	0.115	0.083	0.598	0.500	0.840
3	0.496	0.365	**0.046 (0.368)**	0.653	0.885	0.758
4	0.542	0.501	0.051	0.968	0.631	0.383
5	0.589	0.580	**0.045 (0.368)**	0.873	0.724	0.139
6	0.533	0.476	0.069	0.970	0.443	0.074
DWI b 1000						
0	0.179	**0.049 (0.363)**	**0.027 (0.403)**	0.179	0.352	0.923
2	0.288	0.180	0.085	0.474	0.972	0.613
3	0.655	0.140	**0.020 (0.422)**	0.242	0.925	0.870
4	0.737	0.116	**0.012 (0.455)**	0.194	0.704	0.946
5	0.770	0.075	**0.015 (0.438)**	0.060	0.576	0.902
6	0.722	0.080	**0.009 (0.467)**	0.185	0.961	0.802
ADC						
0	0.306	0.964	**0.017 (0.432)**	0.306	0.968	0.466
2	0.473	0.327	**0.011 (0.457)**	0.142	0.052	0.154
3	0.551	0.964	**0.011 (0.457)**	0.214	0.122	0.085
4	0.551	0.529	**0.012 (0.452)**	0.580	0.157	**0.036 (0.385)**
5	0.378	0.445	**0.009 (0.469)**	0.161	**0.028 (−0.401)**	0.695
6	0.329	0.683	**0.013 (0.448)**	0.064	**0.017 (−0.434)**	0.743
T1WI						
0	0.707	0.076	0.071	0.707	0.181	0.087
2	0.840	0.783	0.514	0.853	0.857	0.571
3	0.188	0.982	0.733	0.818	0.783	0.832
4	0.117	0.985	0.526	0.826	0.557	0.752
5	0.146	0.901	0.693	0.645	0.111	0.822
6	0.094	0.715	0.901	0.423	0.195	0.727
CM phase						
0	0.168	0.164	0.291	0.168	**0.020 (0.530)**	0.213
2	**0.004 (−0.626)**	0.085	0.261	**0.034 (−0.489)**	0.352	**0.038 (0.480)**
3	**0.002 (−0.661)**	0.054	0.310	**0.013 (−0.556)**	0.855	0.181
4	**0.002 (−0.662)**	0.135	0.393	**0.014 (−0.555)**	0.940	0.368
5	**0.002 (−0.654)**	0.101	0.372	**0.007 (−0.597)**	0.849	0.118
6	**0.002 (−0.663)**	0.086	0.371	**0.014 (−0.555)**	0.549	**0.023 (0.518)**
NG phase						
0	0.206	0.385	0.864	0.206	0.067	0.626

Table 4 (continued)

SSF	Mean	SD	Entropy	MPP	Skewness	Kurtosis
2	**0.019 (−0.519)**	0.100	0.703	**0.015 (−0.537)**	0.997	0.087
3	**0.021 (−0.512)**	**0.040 (−0.462)**	0.507	**0.012 (−0.552)**	0.580	0.064
4	**0.008 (−0.572)**	**0.023 (−0.506)**	0.523	**0.004 (−0.612)**	0.511	0.132
5	**0.006 (−0.596)**	**0.009 (−0.567)**	0.541	**0.001 (−0.673)**	0.967	0.405
6	**0.003 (−0.627)**	**0.022 (−0.507)**	0.672	**0.001 (−0.683)**	0.409	0.275

Parameters showing statistical significance ($P < 0.05$) are highlighted in bold with the corresponding correlation coefficient (ρ) in parentheses

level. However, against expectation, the SD values of high-grade tumors were lower than those of low-grade tumors on the NG phase images.

In summary, our study yielded several individual texture parameters which demonstrated good performance in differentiating CC-RCC from NC-RCC and high-grade from low-grade CC-RCC. Best differentiation for both type and grade was achieved on the CM phase using SSF 3. An effort was made to remove the confounding effect of macroscopic necrosis by excluding such areas from ROI analysis, so that the texture parameters truly reflect heterogeneity at the microscopic level. However, texture analysis is an emerging field and the exact basis for the translation of texture data to histologic findings is not yet completely understood. In addition, challenges like the need for uniform acquisition protocols and reproducibility across vendors and institutions are to be met. However, in the future, if definite evidence becomes available and the hurdles could be mitigated, automated or semi-automated TA could serve as an adjunct quantitative tool to morphologic assessment of renal lesions. At present, histological assessment of the biopsy or surgical specimens remains the gold standard tool for predicting tumor aggressiveness and guiding therapeutic decisions.

Our study had few limitations. First, our sample size of 34 tumors was small with skewed distribution of the different subgroups. Second, we acknowledge that although MRI provides multiple paradigms as compared to CT; the reproducibility of MRTA is less owing to lack of standardized acquisition protocols. Third, we assessed only first-order statistical texture parameters. Higher-order statistical parameters may provide more dimensions of data; but on the other hand, the large volume of data generated makes data reduction more computationally intensive. In addition, the biologic basis for many of the higher-order statistical parameters is not yet known. Finally, a combination of texture parameters, as with machine learning, may be more useful in classifying lesions rather than individual parameters since it summates and enhances subtle findings from the different component parameters [13, 17]. We could not incorporate machine learning or deep learning techniques in our study due to the small, skewed sample. But machine learning or algorithm-based combinations may not always be productive since they may undermine the biologic basis of individual parameters.

In conclusion, MR texture analysis revealed several parameters with excellent diagnostic performance (AUC > 0.8) in differentiating CC-RCC from NC-RCC, and high-grade from low-grade CC-RCC. MR texture analysis can potentially serve as a useful non-invasive tool in subtyping and grading RCC. However, histopathology still remains the gold standard in the current clinical practice. Larger validation studies are needed before TA can be adopted in routine radiology practice.

Table 5 Mann–Whitney U test in the differentiation of high-grade CC-RCC from low-grade CC-RCC: *P* value of all the evaluated texture parameters, listed MR sequence-wise

SSF	Mean	SD	Entropy	MPP	Skewness	Kurtosis
T2WI						
0	0.448	1.000	0.746	0.448	0.713	**0.049**
2	**0.039**	0.214	0.650	0.109	0.588	0.100
3	0.248	0.183	0.619	0.231	0.248	0.350
4	0.812	0.120	0.812	0.328	0.155	0.530
5	0.948	0.198	0.983	0.588	0.373	0.231
6	0.948	0.214	0.914	0.502	0.880	0.350
DWI b 500						
0	**0.035**	0.328	0.120	**0.035**	0.779	0.713
2	0.812	0.143	0.100	0.713	0.948	0.422
3	0.746	0.307	0.061	0.559	0.619	0.559
4	0.812	0.475	0.074	0.846	0.948	0.530
5	0.880	0.559	0.061	1.000	0.559	0.328
6	0.812	0.475	0.109	0.948	0.248	0.183
DWI b 1000						
0	0.067	0.074	**0.039**	0.067	0.475	0.948
2	0.448	0.100	**0.049**	0.307	0.650	0.746
3	1.000	0.074	**0.010**	0.120	0.559	0.983
4	0.914	**0.039**	**0.003**	0.082	0.422	0.713
5	0.880	**0.024**	**0.005**	**0.019**	0.448	0.746
6	0.880	**0.024**	**0.003**	0.061	0.983	0.948
ADC						
0	0.131	0.650	**0.028**	0.131	0.846	0.143
2	0.373	0.155	**0.019**	**0.049**	**0.044**	0.131
3	0.373	0.983	**0.019**	0.100	0.074	**0.028**
4	0.373	0.530	**0.019**	0.422	0.198	**0.017**
5	0.267	0.397	**0.017**	0.248	0.061	0.502
6	0.267	0.502	**0.022**	0.074	**0.035**	0.812
T1WI						
0	0.677	**0.023**	**0.020**	0.677	0.187	0.152
2	1.000	0.522	0.276	0.559	0.803	0.598
3	0.276	0.598	0.329	0.487	0.846	0.637
4	0.276	0.559	0.169	0.677	0.718	0.846
5	0.388	0.522	0.229	0.846	0.108	1.000
6	0.329	0.677	0.357	0.890	0.108	0.846
CM phase						
0	0.278	0.211	0.278	0.278	**0.043**	0.497
2	**0.003**	0.182	0.243	0.079	0.549	0.065
3	**0.003**	0.156	0.278	**0.043**	0.968	0.278
4	**0.004**	0.278	0.315	**0.035**	0.780	0.447
5	**0.006**	0.182	0.356	**0.022**	0.661	0.182
6	**0.006**	0.156	0.356	**0.035**	0.842	0.053
NG phase						
0	0.353	0.631	0.971	0.353	0.143	1.000
2	**0.029**	0.190	0.684	**0.035**	1.000	0.143
3	**0.035**	0.089	0.436	**0.029**	0.436	0.089
4	**0.015**	**0.043**	0.529	**0.011**	0.315	0.165
5	**0.011**	**0.023**	0.579	**0.004**	0.796	0.393
6	**0.009**	0.052	0.739	**0.005**	0.579	0.218

Parameters showing statistical significance ($P < 0.05$) are highlighted in bold

Table 6 AUC values and diagnostic performance of all the parameters which showed statistical significance ($P < 0.05$) in the differentiation of high-grade from low-grade CC-RCC, listed MR sequence-wise

Parameter	SSF	AUC	Cut-off	Sensitivity	Specificity	PPV	NPV	Accuracy
T2W								
Mean	2	0.735	≤2.170	60.0	90.0	75.0	81.8	80.0
Kurtosis	0	0.723	≥0.620	60.0	95.0	85.7	82.6	83.3
DWI b500								
Mean	0	0.570	≤78.220	30.0	90.0	60.0	72.0	70.0
MPP	0	0.740	≤133.14	60.0	90.0	75.0	81.8	80.0
DWI b1000								
SD	4	0.735	≥26.300	70.0	75.0	58.3	83.3	73.3
SD	5	0.755	≥25.920	80.0	75.0	61.5	88.2	76.7
SD	6	0.755	≥22.220	90.0	60.0	52.9	92.3	70.0
Entropy	0	0.735	≥3.410	60.0	95.0	85.7	82.6	83.3
Entropy	2	0.723	≥3.780	80.0	70.0	57.1	87.5	73.3
Entropy	3	0.790	≥4.140	50.0	100	100	80.0	83.3
Entropy	4	0.823	≥3.980	80.0	80.0	66.7	88.9	80.0
Entropy	5	0.810	≥4.140	70.0	90.0	77.8	85.7	83.3
Entropy	6	**0.823***	≥4.140	70.0	90.0	77.8	85.7	**83.3**
MPP	5	0.765	≥24.910	70.0	75.0	58.3	83.3	73.3
ADC								
Entropy	0	0.748	≥4.920	60.0	85.0	66.7	81.0	76.7
Entropy	2	0.765	≥5.510	50.0	100	100	80.0	83.3
Entropy	3	0.765	≥5.510	50.0	100	100	80.0	83.3
Entropy	4	0.765	≥5.510	50.0	100	100	80.0	83.3
Entropy	5	0.770	≥5.520	50.0	100	100	80.0	83.3
Entropy	6	0.760	≥5.520	50.0	95.0	83.3	79.2	80.0
MPP	2	0.725	≤372.71	90.0	65.0	56.3	92.9	73.3
Skewness	2	0.730	≤−0.030	80.0	65.0	53.3	86.7	70.0
Skewness	6	0.738	≤−0.110	70.0	75.0	58.3	83.3	73.3
Kurtosis	3	0.748	≥−0.100	90.0	60.0	52.9	92.3	70.0
Kurtosis	4	0.770	≥−0.360	100	50.0	50.0	100	66.7
T1W								
SD	0	0.778	≥14.760	66.7	87.5	75.0	82.4	80.0
Entropy	0	0.781	≥3.970	66.7	87.5	75.0	82.4	80.0
CM phase								
Mean	2	**0.889**	≤0.200	88.9	100	100	90.9	94.7
Mean	3	**0.889***	≤7.550	88.9	100	100	90.9	94.7
Mean	4	0.878	≤39.920	88.9	90.0	88.9	90.0	89.5
Mean	5	0.867	≤31.280	77.8	100	100	83.3	89.5
Mean	6	0.867	≤75.030	77.8	100	100	83.3	89.5
MPP	3	0.778	≤67.320	66.7	100	100	76.9	84.2
MPP	4	0.789	≤80.380	66.7	100	100	76.9	84.2
MPP	5	**0.811**	≤113.49	66.7	100	100	76.9	84.2
MPP	6	0.789	≤130.99	66.7	90.0	85.7	75.0	78.9
Skewness	0	0.778	≥−0.110	100	70.0	75.0	100	84.2
NG phase								
Mean	2	0.790	≤7.400	80.0	90.0	88.9	81.8	85.0
Mean	3	0.780	≤25.690	80.0	80.0	80.0	80.0	80.0
Mean	4	0.820	≤9.720	70.0	90.0	87.5	75.0	80.0
Mean	5	0.830	19.260	70.0	90.0	87.5	75.0	80.0
Mean	6	**0.840**	≤31.140	70.0	100	100	76.9	85.0
SD	4	0.770	≤135.91	80.0	80.0	80.0	80.0	80.0
SD	5	**0.800**	≤165.52	90.0	70.0	75.0	87.5	80.0

Table 6 (continued)

Parameter	SSF	AUC	Cut-off	Sensitivity	Specificity	PPV	NPV	Accuracy
MPP	2	0.780	≤71.790	70.0	80.0	77.8	72.7	75.0
MPP	3	0.790	≤93.250	70.0	90.0	87.5	75.0	80.0
MPP	4	0.830	≤125.88	70.0	90.0	87.5	75.0	80.0
MPP	5	**0.870***	≤193.67	90.0	80.0	81.8	88.9	85.0
MPP	6	0.860	≤217.36	90.0	80.0	81.8	88.9	85.0

Parameters remaining after the second step of feature selection are shown in bold. The sequence-wise single best parameters are highlighted with asterisk

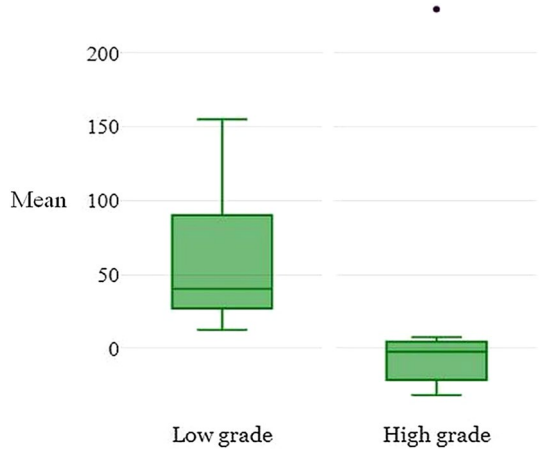

Fig. 4 Box and whisker plot of the best forming parameter in differentiating high-grade from low-grade CC-RCC (mean at SSF3 on the corticomedullary phase)

Author contributions Study concepts and design: AG, AR, DK, RS; Data acquisition: AG, AR, PD; Data analysis and interpretation: AG, AR, DK, BG, RS; Literature research: AG, AR, RS; Manuscript drafting: AG, AR; Manuscript revision for important intellectual content: AG, AR, DK, BG, RS; Approval of the final version of the submitted manuscript: all authors.

Compliance with ethical standards

Conflict of interest One of the authors (Balaji Ganeshan) is a director and part time employee of Feedback Medical Ltd., a UK based company which develops and markets the TexRAD texture analysis software used in this study. All the other authors are from the All India Institute of Medical Sciences, New Delhi, India and certify that we had complete control over the study and the results submitted.

References

1. Bray F, Ferlay J, Soerjomataram I, Siegel RL, Torre LA, Jemal A. Global cancer statistics 2018: GLOBOCAN estimates of incidence and mortality worldwide for 36 cancers in 185 countries. CA Cancer J Clin. 2018 Nov 1;68(6):394–424.
2. Capitanio U, Montorsi F. Renal cancer. Lancet Lond Engl. 2016 Feb 27;387(10021):894–906
3. Volpe A, Patard JJ. Prognostic factors in renal cell carcinoma. World J Urol. 2010 Jun;28(3):319–27
4. Ficarra V, Righetti R, Martignoni G, D'Amico A, Pilloni S, Rubilotta E, et al. Prognostic value of renal cell carcinoma nuclear grading: multivariate analysis of 333 cases. Urol Int. 2001;67(2):130–4
5. Muglia VF, Prando A. Renal cell carcinoma: histological classification and correlation with imaging findings. Radiol Bras. 2015;48(3):166–74
6. Posadas EM, Limvorasak S, Figlin RA. Targeted therapies for renal cell carcinoma. Nat Rev Nephrol. 2017 Jul 10;13:496
7. Corapi KM, Chen JLT, Balk EM, Gordon CE. Bleeding complications of native kidney biopsy: a systematic review and meta-analysis. Am J Kidney Dis Off J Natl Kidney Found. 2012 Jul;60(1):62–73
8. Andersen MFB, Norus TP. Tumor Seeding With Renal Cell Carcinoma After Renal Biopsy. Urol Case Rep. 2016 Sep 25;9:43–4
9. Posadas EM, Figlin RA. Kidney cancer: progress and controversies in neoadjuvant therapy. Nat Rev Urol. 2014 May;11(5):254–5
10. Wu Y, Kwon YS, Labib M, Foran DJ, Singer EA. Magnetic Resonance Imaging as a Biomarker for Renal Cell Carcinoma. Dis Markers [Internet]. 2015 [cited 2019 Apr 8];2015. Available from: https://www.ncbi.nlm.nih.gov/pmc/articles/PMC4644550/
11. Goyal A, Sharma R, Bhalla AS, Gamanagatti S, Seth A, Iyer VK, et al. Diffusion-weighted MRI in renal cell carcinoma: a surrogate marker for predicting nuclear grade and histological subtype. Acta Radiol Stockh Swed 1987. 2012 Apr 1;53(3):349–58.
12. Lubner MG, Smith AD, Sandrasegaran K, Sahani DV, Pickhardt PJ. CT Texture Analysis: Definitions, Applications, Biologic Correlates, and Challenges. Radiogr Rev Publ Radiol Soc N Am Inc. 2017 Oct;37(5):1483–503.
13. Raman SP, Chen Y, Schroeder JL, Huang P, Fishman EK. CT texture analysis of renal masses: pilot study using random forest classification for prediction of pathology. Acad Radiol. 2014 Dec;21(12):1587–96
14. Lubner MG, Stabo N, Abel EJ, del Rio AM, Pickhardt PJ. CT Textural Analysis of Large Primary Renal Cell Carcinomas: Pretreatment Tumor Heterogeneity Correlates With Histologic Findings and Clinical Outcomes. Am J Roentgenol. 2016 May 4;207(1):96–105
15. Kierans AS, Rusinek H, Lee A, Shaikh MB, Triolo M, Huang WC, et al. Textural differences in apparent diffusion coefficient between low- and high-stage clear cell renal cell carcinoma. AJR Am J Roentgenol. 2014 Dec;203(6):W637-644
16. Yu H, Scalera J, Khalid M, Touret A-S, Bloch N, Li B, et al. Texture analysis as a radiomic marker for differentiating renal tumors. Abdom Radiol N Y. 2017;42(10):2470–8
17. Zhang G-M-Y, Shi B, Xue H-D, Ganeshan B, Sun H, Jin Z-Y. Can quantitative CT texture analysis be used to differentiate subtypes of renal cell carcinoma? Clin Radiol. 2019 Apr;74(4):287–94.

18. Bektas CT, Kocak B, Yardimci AH, Turkcanoglu MH, Yucetas U, Koca SB, et al. Clear Cell Renal Cell Carcinoma: Machine Learning-Based Quantitative Computed Tomography Texture Analysis for Prediction of Fuhrman Nuclear Grade. Eur Radiol. 2019 Mar;29(3):1153–63
19. Shu J, Tang Y, Cui J, Yang R, Meng X, Cai Z, et al. Clear cell renal cell carcinoma: CT-based radiomics features for the prediction of Fuhrman grade. Eur J Radiol. 2018 Dec;109:8–12
20. Kocak B, Yardimci AH, Bektas CT, Turkcanoglu MH, Erdim C, Yucetas U, et al. Textural differences between renal cell carcinoma subtypes: Machine learning-based quantitative computed tomography texture analysis with independent external validation. Eur J Radiol. 2018 Oct 1;107:149–57
21. Vendrami CL, Velichko YS, Miller FH, Chatterjee A, Villavicencio CP, Yaghmai V, et al. Differentiation of Papillary Renal Cell Carcinoma Subtypes on MRI: Qualitative and Texture Analysis. Am J Roentgenol. 2018 Sep 21;211(6):1234–45
22. Miles KA, Ganeshan B, Hayball MP. CT texture analysis using the filtration-histogram method: what do the measurements mean? Cancer Imaging. 2013 Sep 23;13(3):400–6
23. Hodgdon T, McInnes MDF, Schieda N, Flood TA, Lamb L, Thornhill RE. Can Quantitative CT Texture Analysis be Used to Differentiate Fat-poor Renal Angiomyolipoma from Renal Cell Carcinoma on Unenhanced CT Images? Radiology. 2015 Sep;276(3):787–96
24. Vikram R, Ng CS, Tamboli P, Tannir NM, Jonasch E, Matin SF, et al. Papillary Renal Cell Carcinoma: Radiologic-Pathologic Correlation and Spectrum of Disease. RadioGraphics. 2009 May 1;29(3):741–54
25. Woo S, Suh CH, Kim SY, Cho JY, Kim SH. Diagnostic Performance of DWI for Differentiating High- From Low-Grade Clear Cell Renal Cell Carcinoma: A Systematic Review and Meta-Analysis. Am J Roentgenol. 2017 Oct 12;209(6):W374–81